

A Method for IR Measurement of Large Scale Roughened Surfaces in Hypersonic Flow

Wesley Condren* Christopher Hambidge[†] David Steuer[‡] Imran Naved[§] Matthew McGilvray[¶]
Oxford Thermofluids Institute, University of Oxford, Oxford, England OX2 0ES, United Kingdom

This paper presents a methodology for adapting the Infrared Thermography (IRT) diagnostic technique for use on large scale rough surfaces. Situations where more established methods of surface heat transfer measurement, such as thin film gauges (TFG) and calorimeter gauges, are typically employed are met with a considerable challenge when applied to rough walls. In order for the gauges to provide meaningful data, their surface must possess the same topography as the surrounding roughness, which adds to the complexity and expense of gauge construction. Thus, a benefit of IRT over gauge methods is IRT's ability to provide data in a non-intrusive manner that is easily adapted to any roughness geometry, reducing the necessity for a multitude of different gauges. Furthermore, IRT produces spatially continuous heat transfer data over a given surface area, providing insight into the heat flux augmentation that rough walls experience. This methodology also solves the general problem that arises from the change in directional emissivity that accompanies the varying surface height of rough walls. As this is a consequence of 3D effects, the 2D image produced by IRT does not inherently account for this and so an emissivity map must be evaluated and given as an input. The methodology in this paper is then applied to an idealised two-dimensional roughness pattern and a three-dimensional pattern that represents an ablated surface of HEEET material developed by NASA, showcasing the Stanton number enhancement maps and emissivity maps produced.

I. Nomenclature

α	=	Absorptivity Coefficient
ε	=	Emissivity
ρ_r	=	Reflectivity Coefficient
τ	=	Transmissivity Coefficient
θ	=	Angle Relative to Surface Normal
λ	=	Wavelength
γ	=	Ratio of specific heats
I	=	Radiance
n	=	Refractive Index
T	=	Temperature
p	=	Pressure
M	=	Mach number
u	=	Velocity
ρ	=	Density
Re_x	=	Unit Reynolds number

II. Introduction

In recent years, the capabilities of space travel have expanded, pushing deeper into space with missions prospected to reach Saturn, Jupiter and Uranus. Additionally, the development of scram-jets could provide means of sustained

*DPhil Candidate, Department of Engineering Science, University of Oxford.

[†]Postdoctoral Research Assistant, Department of Engineering Science, University of Oxford

[‡]Research Assistant, University of Oxford

[§]Research Assistant, University of Oxford

[¶]Associate Professor, Department of Engineering Science, University of Oxford

hypersonic flight. In either case, the movement of a vehicle at speeds greater than Mach 5 through an atmosphere, be it an extra-terrestrial one or our own, is inescapable and presents a fundamental problem to hypersonic flight. The interaction between the surrounding atmosphere and the hypersonic vehicle creates an extremely hostile environment as the vehicle's kinetic energy is converted to the flow's internal energy. The temperatures realised are high enough to ionise the gaseous atoms and severely damage the material the vehicle is composed of. To maintain the structural integrity of the vehicle, some means of thermal protection is required.

Ablative heat shields are a commonly applied thermal protection system (TPS). They are a semi-passive technology where an additional layer of material coats the outer surface of the vehicle. This material, when subject to high temperatures, undergoes pyrolysis, producing a porous char layer and gaseous products. Over time, this layer sublimates and recesses. Both the energy transferred away from the vehicle by this process and the cooling provided by the injection of relatively cold pyrolysis gases passing through the char layer keep the temperatures of the outer surface below critical values. The function of ablatives inherently produces a rough surface; as the material ablates away from the vehicle, it leaves behind artifacts with roughness heights such that they protrude into the high-speed flow outside the boundary layer. As a consequence, the ablated surface experiences an augmentation in the convective heat flux incident to it, typically increasing it above smooth wall levels [1]. As a result, the categorisation and prediction of this heat flux augmentation is imperative, as it effects the subsequent behaviour of the ablative material and thus the design of an installation of the TPS prior to flight.

There have been experimental efforts to categorise rough wall effects, dating back to the 1930s with the pioneering experiments conducted by Nikuradase [2] using sand and the expansion of this work to general rough surfaces by Schlichting [3]. Schlichting introduced the idea of equivalent sand grain roughness defined as the height of Nikuradase sand that would recreate same effect on the flow field as a given roughness geometry. Further expanding on this idea, a number of semi-empirical correlations that consolidate a multitude of geometric factors into a single shape parameter used to find a rough surface's equivalent sand grain height were developed [4] [5] [6]. Many of the findings proposed by these early works have been used to analyse subsequent projects into rough wall behaviour but an issue is met when beginning to analyse large-scale roughened surfaces in hypersonic flow fields like those produced by ablative materials. The problem is that the established correlations for predicting rough wall effects were developed primarily through experimentation at subsonic speeds. At these low speeds, flow behaviour over the roughness elements differs greatly from its supersonic and hypersonic counterparts. Furthermore, the geometries used to develop the correlations aren't necessarily representative of surface topography generated by ablative heat shields. This presents an unfortunate limitation to the current methods of prediction and thus research into large scale roughened surfaces specifically in hypersonic conditions are required.

Of the literature pertaining to rough wall effects, very few studies relate specifically to those effects under hypersonic conditions, and of those few, the work by Holden et.al. occupy the majority. A review of the work can be found in Ref. [7]. The main methodology used to acquire the heat flux measurements during this campaign were calorimeter gauges and thin film instrumentation. To provide meaningful data, the gauge surface must be representative of the roughness geometry in question. This constitutes to extremely difficult, expensive, and time-consuming work that can only be used for a single surface topography; should multiple geometries be required, a different gauge must be manufactured. Furthermore, calorimeter and thin film gauges (TFG) only collect data for a discrete point on the surface, and so more than one gauge is necessary to grasp the full picture, quickly multiplying the aforementioned expense and difficulty. This paper alleviates this issue met by traditional means of heat flux measurement and provides a methodology to adapt the novel technique of infrared thermography (IRT), previously applied to smooth, transpiration cooled walls [8], as a means of acquiring heat flux measurements for hypersonic large scale roughness studies. The main advantage of IRT is that it provides non-intrusive, spatially continuous data and can be applied to any roughness geometry. The method addresses the directional dependence of emissivity and the implications of this on rough walls. Additionally, results of the method are showcased for three dimensional and two-dimensional roughness geometries subject to hypersonic flow conditions with a comparison of the methods output to thin film gauge data alongside details of the experimental set up and procedures.

III. Infrared Thermography

The technique hinges off Planck's law of radiation, relating the radiance emitted from a body to its temperature. Unavoidably, the emitted radiation that reaches the camera's sensing element is not purely from the desired object; unwanted radiance emitted by the surroundings also reaches the camera, augmenting the recorded intensity values. Furthermore, the radiance does not immediately reach the sensor; the electromagnetic waves must propagate through

the surrounding atmosphere and through any material, such as a window, between the camera and the body. This results in a further augmentation to the intensity values, as each material has its own propensity to absorb, transmit and reflect the radiance from the desired object. To account for these effects, a multi-point calibration process must be performed for each IR camera view with a black body calibrator [9]. This calibration process removes the necessity of knowing the absorption and transmission coefficients of all the intermediate material, reducing the required material inputs to merely the emissivity and thermal effusivity of the object in question [10] [11]. The emissivity of a material poses a challenge when applying IR thermography to rough surfaces. This property is a function of the view angle relative to the surface normal, which on a 3D surface can potentially exceed angles greater than 50° , resulting in significant changes to the material emissivity. Consequently, data collected along the surface of a roughness element with IR must account for these effects to avoid significant under- or overestimation of heat flux values. The method described below provides the means to do so.

A. Fundamentals of IRT

Radiation can be absorbed, reflected, and transmitted from a body. Defining the absorptivity, reflectivity, and transmissivity coefficients as the fraction of radiation that is absorbed, reflected, and transmitted by the body respectively and then applying the law of the conservation of energy, the following relation between the three is obtained Eq. (1) [12].

$$\alpha + \rho_r + \tau = 1 \quad (1)$$

The materials used for IRT are usually opaque, meaning that their transmission coefficient falls to zero. Furthermore, at thermal equilibrium, the radiation absorbed by the body is equal to that which is emitted by the body altering Eq. (1) to Eq. (2)[12].

$$\varepsilon + \rho_r = 1 \quad (2)$$

Here, the emissivity ε , is defined as the ratio of the radiance emitted by the material to that emitted by a black body ($\varepsilon_{bb} = 1$) at the same temperature.

This quantity feeds into the IR camera data analysis when considering the total radiance from the object that reaches the camera's sensing element after applying the simplifications provided by the multi-point calibration process. The total radiance captured, I_D , is the sum of the radiance emitted by the object $\varepsilon \cdot I_{bb}$ and the fraction of the ambient radiance I_{Amb} that the object reflects shown in Eq. (3)[13].

$$I_D = \varepsilon \cdot I_{bb} + \rho_r \cdot I_{Amb} \quad (3)$$

Where I_{bb} refers to the radiance emitted by a black body at the same temperature as the object defined by Planck's law of radiation defined in Eq. (4) [12].

$$I_{bb} = \frac{C_1}{\lambda^5 \cdot (e^{C_2/\lambda T} - 1)} \quad (4)$$

Where C_1 and C_2 are the first and second universal constants equal to $3.7418 \times 10^{-16} Wm^{-2}$ and $1.4388 \times 10^{-2} mK$ respectively. Typical cameras operate within a fixed wavelength range, and, thus, a semi-empirical relation between the in-band radiance (radiance emitted within this fixed wavelength range) and temperature can be found specific to the camera used defined in Eq. (5) [14].

$$I_{bb,ib} = \frac{R}{e^{B/T} - F} \quad (5)$$

Where the constants R, B and, F are fitting parameters for a particular camera.

I_{bb} is directly related to the body's temperature, and thus rearranging Eq. (3) and then the camera specific Planck's law in Eq. (5) the temperature of the body can be found and thus the heat flux it experienced.

B. Theoretical Emissivity Evaluation

As stated previously, the emissivity, ε , is a function of the angle, θ relative to the body's surface normal. In general, the emissivity of a material is a function of both direction and wavelength. However, it is assumed that over the finite wavelength range of typical IR cameras at low temperatures, the variation of emissivity with wavelength can be neglected, leaving only the directional dependence. This dependence, for an opaque, non-magnetic dielectric material, can be defined theoretically by the following correlation [15] shown in Eq. (6).

$$\varepsilon(\theta) = \frac{2\cos(\theta) \cdot \sqrt{n^2 - \sin^2(\theta)}}{\left(\cos(\theta) + \sqrt{n^2 - \sin^2(\theta)}\right)^2} \cdot \left(1 + \frac{n^2}{\left(\cos(\theta) \cdot \sqrt{n^2 - \sin^2(\theta)} + \sin^2(\theta)\right)^2}\right) \quad (6)$$

Where n is the refractive index of the material and θ is in radians.

When situated normal to the surface Eq. (6) collapses to the following function of n alone in Eq. (7).

$$\varepsilon(\theta = 0) = \frac{4n}{(n + 1)^2} \quad (7)$$

The variation of emissivity with angle is shown for various dielectric materials in Fig. 1(a).

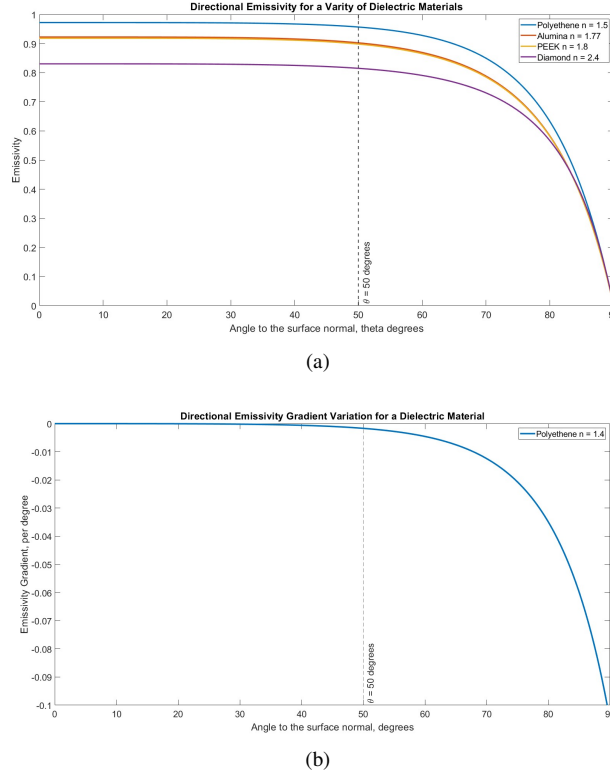


Fig. 1 (a) Variation of emissivity of a dielectric material for varying refractive indices. (b) Variation of directional emissivity gradient of a dielectric material with refractive index $n = 1.4$.

It can be seen from Fig. 1 that the emissivity of insulating materials remains mostly constant until θ reaches 50 degrees changing by an insignificant 2% across all refractive indices plotted. This remark is seconded by the emissivity gradient curve reaching only -0.001 per degree at the 50 degree point shown in Fig. 1(b). Comparatively, after this point a much steeper change is observed — for example, when $n = 1.4$ a decrease by 11% occurs over a much smaller angle change of 20 degrees. Additionally, a decrease in the emissivity normal to the surface is shown with an increase in refractive index.

C. Experimental Emissivity Evaluation

This is a theoretical model and thus assumes an ideal unblemished surface. In reality, there may be artifacts present on the surface, such as a surface finish, which would inevitably introduce deviations from the theoretical result, creating the need for evaluating the directional emissivity of the real material. This is of key importance when dealing with 3D printed surfaces, which allow the production of more intricate roughness geometries, as surface finish and material properties can vary batch to batch.

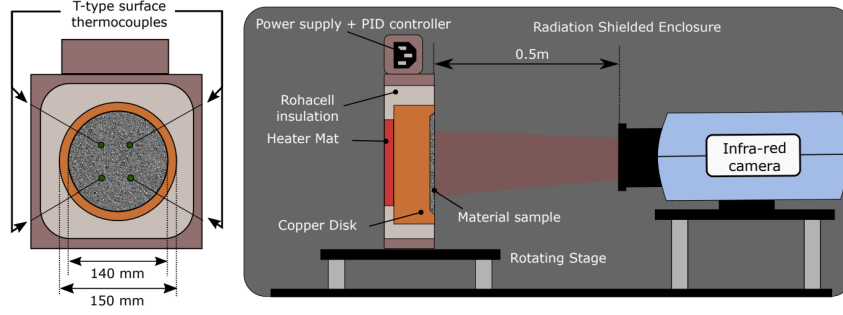


Fig. 2 Schematic of the in-house bench-top emissivity measurement setup, not to scale [11].

1. Experimental Set up

The experimental set up to evaluate the directional emissivity $\varepsilon(\theta)$ in house for a given material is shown in the schematic in Fig. (2) using an IR camera. The sample used for the calibration is constructed from the desired material in the shape of a circular disk 150mm in diameter and 2mm in thickness to ensure that the IR camera's field of view is within the material surface area and to reduce the time taken to reach thermal equilibrium over this area. This sample will then be bonded to a 20mm thick copper disk of the same diameter with a highly conductive thermal paste and instrumented with a surface mounted thermocouple. The copper heating element is encased in Rohacell, reducing the energy losses via conduction, and its temperature will be controlled with a PID controller, keeping its temperature steady within $\pm 0.1K$. Lastly, the target and camera will be placed in a shielded environment to reduce the sources of radiance detected by the camera to that of the object and the reflections off the object from the radiation shield walls and internal atmosphere.

2. Experimental Procedure

Once set up, the first step of the experimental procedure as it stands is to heat the element to a desired temperature T_1 letting both it and the material target temperature reach a steady state. Once the temperature is reached, the camera will record N frames, normal to the material surface ($\theta = 0$), over which the radiance captured can be averaged. Utilising Eq. (3) and the camera specific Planck's law Eq. (5), the relationship between the radiance captured and that emitted from the body can be constructed as shown in Eq. (8).

$$I_{D1}(T_1, \theta) = \varepsilon_{obj}(\theta) \cdot \frac{R}{e^{B/T_1} - F} + (\rho_{obj} \cdot \varepsilon_{env} + \rho_{obj} \varepsilon_{wall}) \cdot \frac{R}{e^{B/T_{amb}} - F} \quad (8)$$

It is noted that Eq. (8) adds an additional two unknowns in the form of the emissivity of the shielding, ε_{wall} , and that of the surrounding environment, ε_{env} . However, it is assumed that the ambient temperature remains constant, so by taking a second reading at a higher temperature T_2 and then taking the difference between the captured radiance at each instance, the unknowns are reduced back down to one — the emissivity of the material in question ε_{obj} shown in Eq. (9).

$$I_{D1}(T_2, \theta) - I_{D1}(T_1, \theta) = \varepsilon_{obj}(\theta) \cdot \left(\frac{R}{e^{B/T_2} - F} - \frac{R}{e^{B/T_1} - F} \right) \quad (9)$$

The surface mounted thermocouple on the material will allow the determination of the true object temperature, which at steady state will be a uniform temperature T_1 and then T_2 . Assuming the body was a perfect emitter, the difference in radiance captured by the camera at the two instances would be as stated in Eq. (10).

$$I_{D2}(T_2, \theta) - I_{D2}(T_1, \theta) = \frac{R}{e^{B/T_2} - F} - \frac{R}{e^{B/T_1} - F} \quad (10)$$

Taking the ratio of these of Eq.(9) to Eq. (10) will then produce the emissivity of the material shown in Eq. (11). The angle of the camera relative to the surface is adjusted by rotating the material target, after which, the proceedings detailed above are repeated, describing the functional relationship between the material emissivity and angle.

$$\varepsilon_{obj}(\theta) = \frac{I_{D1}(T_2, \theta) - I_{D1}(T_1, \theta)}{I_{D2}(T_2, \theta) - I_{D2}(T_1, \theta)} \quad (11)$$

IV. Evaluation of Camera View Angle

As stated prior, the emissivity of the material has a directional dependence of the from shown in Fig. 1. The value of theta is the view angle of the camera, θ_v and this value, due to its influence on material emissivity, affects the magnitude of the IR signal. In the context of large-scale roughness studies, accurate camera angle measurements are of greater importance, as the surface topography can push the view angles to values greater than 50° , after which small angle changes significantly affect the material's emissivity.

In this work, the view angle is decomposed into two angles, the angle made between a ray joining the camera to a point on the flat surface and its surface normal θ_{flat} and then surface normal of the rough surface θ_{Rn} shown in Eq. (12).

$$\theta_v = \theta_{flat} \pm \theta_{Rn} \quad (12)$$

where θ_{Rn} either reduces the view angle making the camera more normal to the surface or vice versa.

As the 3D geometry of the roughness surface was known accurately a priori, and thus θ_{Rn} , the problem is reduced to the evaluation θ_{flat} , a well-known problem in the field of optics. This evaluation requires the position of the camera relative to the flat plate model, or pose of the IR camera, to be known.

A. Evaluation of the camera intrinsic parameters & camera pose

The conversion of 3D coordinates to a 2D dimensional pixel map that occurs when an image is captured using any camera can be separated into two parts. During the first part, the imaged object's coordinates in the world frame of reference are converted to coordinates relative to the camera. This process is controlled by the extrinsic parameters of the set-up, depending solely on the position and orientation of the camera used. During the second part, three-dimensional coordinates relative to the camera are converted to two-dimensional image coordinates. This coordinate manipulation is governed by the camera's intrinsic parameters that pertain to camera properties that effect the how the image is captured. To be able to determine an optical set-up's intrinsic and extrinsic parameters, another calibration process is required. The calibration method adopted for the purposes of this work is one put forward by Heikkila and Silvén [16]. This method assumes a pinhole camera model, which is an idealised model that defines the relationship between the three-dimensional coordinates of a point in the world frame of reference to the two dimensional coordinates of its projection onto the image plane. The model is showcased in Fig. 3 and the relationship between a general object point P to its projection is defined by Eq. (13).

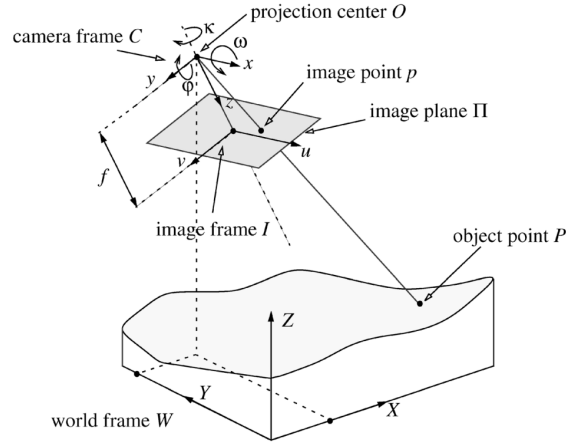


Fig. 3 Pinhole camera model of a camera imaging a general point P showcasing the three frames of reference [17]

$$\begin{bmatrix} u & v & 1 \end{bmatrix} \propto \begin{bmatrix} X & Y & Z & 1 \end{bmatrix} \begin{bmatrix} R \\ t \end{bmatrix} K \quad (13)$$

Where K is a 3 by 3 matrix containing the intrinsic camera parameters, R and t are a rotation matrix representing the three-dimensional orientation of the camera and a translation vector of the camera relative to the world frame of

reference, respectively. X , Y and Z are the coordinates of the point P in the world coordinate system and u and v are the image coordinates in pixels.

As the name suggests, the pinhole method assumes the camera aperture is a single point with no focusing of light through a lens, and thus fails to account for the nonlinear distortions injected into the optical path. Consequently, the resulting images are distorted by the lens in real cameras. The distortion introduced can be sectioned into two components, radial and tangential distortion. The pinhole camera model provides the image coordinates undistorted, as the model assumes that the light travelled linearly through the optical centre. The relationship between the undistorted coordinates and the distorted coordinates, $[u_d \ v_d]^T$, observed in the image captured by the camera can be approximated as shown in Eq. (14).

$$\begin{bmatrix} u_d \\ v_d \end{bmatrix} \approx \begin{bmatrix} u \\ v \end{bmatrix} - \boldsymbol{\eta}_d \quad (14)$$

Where $\boldsymbol{\eta}_d$ is defined by Eq. (15).

$$\boldsymbol{\eta}_d = \frac{1}{4k_1r^2 + 6k_2r^4 + 8p_1\bar{v} + 8p_2\bar{u} + 1} \cdot \begin{bmatrix} \bar{u}(k_1r^2 + k_2r^4 + \dots) + (2p_1\bar{u}\bar{v} + p_2(r^2 + 2\bar{u}^2))(1 + p_3r^2 + \dots) \\ \bar{v}(k_1r^2 + k_2r^4 + \dots) + (2p_2\bar{u}\bar{v} + p_1(r^2 + 2\bar{v}^2))(1 + p_3r^2 + \dots) \end{bmatrix} \quad (15)$$

Where $[\bar{u} \ \bar{v}]^T$ is the vector from the optical centre to the undistorted image point, r is the length of that vector and the coefficients $k_1 - k_n$ and $p_1 - p_n$ are the radial and tangential distortion coefficients respectively. The number of coefficients used to encapsulate the distortion depends on its severity. Should large radial and/or tangential distortions be present, then a larger number is required, and vice versa. For the purposes of camera calibration with a non-wide-angle lens, two coefficients suffice. For a more in-depth formulation, refer to the work laid out in Ref. [17] by Heikkila.

The distortion coefficients and the intrinsic matrix \mathbf{K} that contains the focal length, image principal point, and image skew define the camera's intrinsic parameters along with the image size in pixels. The rotation matrix \mathbf{R} and translation vector \mathbf{t} are the extrinsic parameters. These are then solved for by first assuming the distortion is negligible (and thus using linear methods), providing the initial estimate of the intrinsics and extrinsics that is then fed into a nonlinear least-squares minimization as an initial guess for estimating all of the parameters [16] [18].

To provide a solution via the method above, various images of a calibration target are required at various orientations relative to the camera across its full FoV. For cameras that operate in the visible spectrum, a black and white checkerboard or a grid of black circular markers is adopted. For an IR camera these images are not sufficient, as there isn't a strong contrast between the black ink and white paper when imaged in the IR spectrum, and the chosen pattern will therefore not present as clearly. To achieve a strong contrast, there must be a strong emissivity difference between the control points and their surroundings and/or a not insignificant temperature difference between the two. The design considerations for developing such a target are laid out in Cardone et.al [19]. The paper proposes the use of a circular grid composed of holes drilled into a block of aluminium 4 – 5 times the pixel resolution of the camera with a depth of more than 4 times this value. When the block is heated, due to the internal reflections of the IR radiation, the markers present significantly brighter than the reflective surface of the aluminium.

The extrinsic parameters obtained from the methodology above detail the orientation and location of the camera relative to the calibration images and not relative to the orientation and location of the surface roughness as it would be during a test. As a result, separate images of the target in the same plane as the rough surface during a test are required to obtain the relevant extrinsic parameters. To evaluate the position of the camera relative to these images, the location of the markers must be known in both the world frame of reference and in the image frame. For the former, as the holes are regularly spaced in both directions, setting the origin as any one marker allows for the determination of the position of all other markers in the world frame of reference. For the latter, feature detection algorithms can be used to define their location in pixels. With these coordinates and the intrinsic parameters calculated above, the camera pose can be found as a solution to the perspective-n-point problem with a perspective-three-point algorithm [20].

B. Evaluation of the θ_{flat} distribution

With the camera location in the world frame of reference known, the angle of the camera to each of the marker centres can be found through the simple rearrangement of the dot product of a vector joining the camera to the centre of the marker ($\mathbf{v}_{ray}(x, y)$) and the flat plane normal (\mathbf{n}_{plane}) shown in Eq. (16).

$$\theta_{flat}(x, y) = \text{acos} \left(\frac{\mathbf{v}_{ray}(x, y) \cdot \mathbf{n}_{plane}}{|\mathbf{v}_{ray}(x, y)| |\mathbf{n}_{plane}|} \right) \quad (16)$$

Completing this for each of the markers for both IR views provides the angle data at the location of the marker centres. The data obtained, at this stage, consists of a series of scattered points; thus, to determine the angle of the camera in between the markers, interpolation is required, with the triangulation-based linear interpolation method evaluating the angles between marker centres. It is important that the area occupied by the detected control points covers the majority of the camera's FoV, if not full FoV. This limits the area over which the data needs to be extrapolated as this can inject non-physical artifacts.

C. Determination of pixel location on roughness pattern

The section of the roughness element that a pixel is imaging determines the value of θ_{Rn} that will augment the value of θ_{flat} at that location. Therefore, it is important to have a method to identify the section of the roughness pattern that a pixel is observing. The method described here utilises the fact that a roughness pattern will experience a varied degree of heating over its surface as the flow travels across it. The sections of the pattern that protrude higher into the flow field will experience a larger degree of heating as they are subject to hotter, faster moving flow compared to those at lower heights or in a trough. The separation regions produced behind large-scale roughness elements and cavity flow phenomena shield the surface, suppressing the heating they experienced. Consequently, the height of the pattern can be correlated to the relative magnitude of the signal revived by the IR camera, and the height, due to the geometry, can be related to surface angle. This finding then allows the determination of what section of the roughness pattern the data from the IR camera refers to and thus the relevant surface angle θ_{flat} . It is of note that the form of the IR signal used to find the relative magnitudes over the roughness elements referred to earlier can be the radiance, temperature, or the non-emissivity corrected heat flux data. Due to the post-processing required to evaluate the heat flux from the temperature signal, the non-emissivity corrected heat flux data is a stabler measurement for defining the relative magnitudes, as any noise present in the temperature or radiance signals is filtered out.

V. Experimental Set Up

A. High Density Wind Tunnel

The experiments were conducted in the High Density Tunnel (HDT), a heated Ludwig tunnel, at the Oxford Thermofluids Institute. The HDT is a low enthalpy short duration facility with the capability to produce high unit Reynolds number flows typically ranging between Mach 4 and 7. When operating in Ludwig mode, HDT produces several periods of the order of tens of milliseconds during which steady total pressure and unit Reynolds numbers are observed. Figure. 4 shows the tunnel with a conical model in the test section. A more thorough breakdown of the operation and function of HDT can be found in [21] [22].

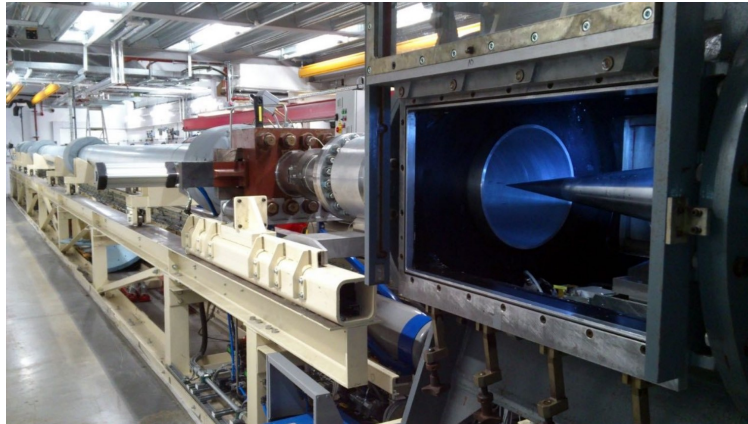


Fig. 4 The Oxford High Density Tunnel featuring a conical model.

B. Model Design

The model used for the experiments consisted of a flat plate shown in Fig. 5 with dimensions 575x260x60mm. The plate housed an interchangeable test piece with an area of 290x90mm and a boundary layer trip located 205mm and 67.5mm downstream of the sharp leading edge respectively. Preceding the test piece and after, the boundary layer trip situated a thin film gauge array to allow the identification of the state of the boundary layer prior to its interaction with the test piece. Both the TFG array and the test piece were centred on the flat plates mid point in the traverse direction. The width of the plate is such to maximise the flow area unaffected by edge effects over the rough surfaces. The point of contamination was identified using surface pressure sensors positioned adjacent to the test piece.

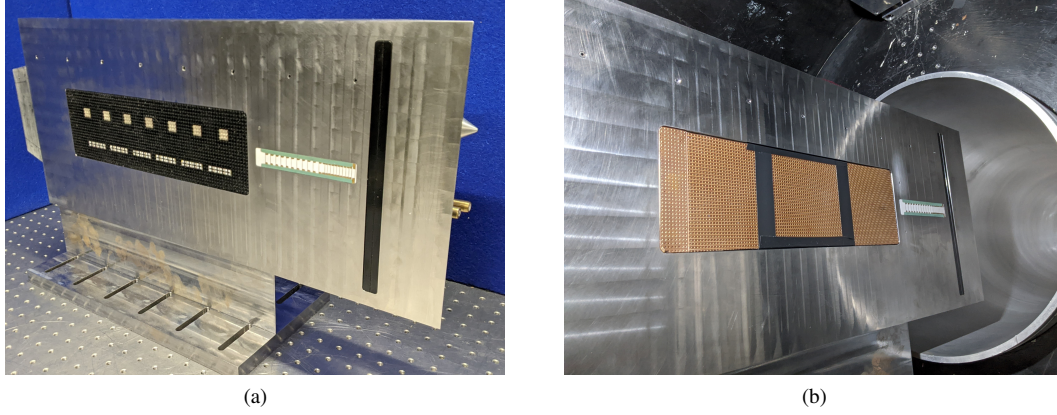


Fig. 5 (a) Front view of the flat plate model showcasing the surface instrumentation, test piece and boundary layer trip.(b) Flat plate model inside the HDT test section with the IR target in place.

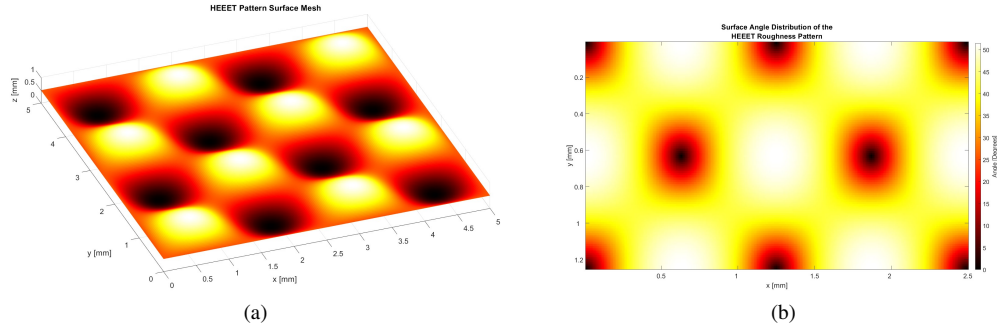


Fig. 6 (a) Idealised HEEET roughness pattern.(b) Surface angle distribution of a single peak and trough pair.

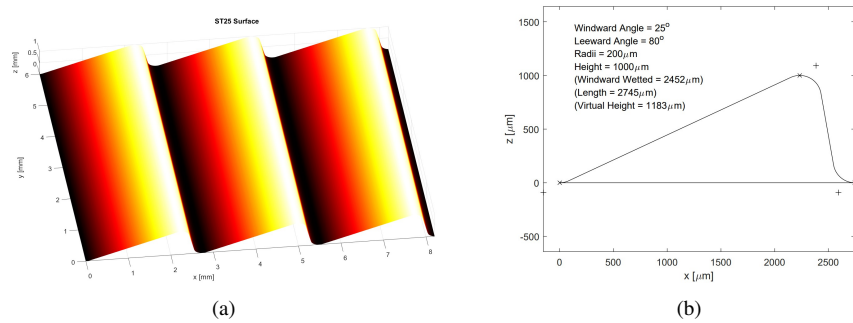


Fig. 7 (a) ST25 roughness pattern surface.(b) ST25 dimensions and angles.

The rough surfaces were generated by a Stratasys Objet30 Polyjet 3D printer with a $40\mu\text{m}$ resolution using VeroBlack resin with a 'gloss' finish. The material properties of VeroBlack required for the IR measurements are displayed in Table. 1. Figure. 6 shows the directional dependence of its emissivity evaluated using the experimental procedure laid out in Section III.C.2. The roughness geometries used to demonstrate the method are an idealised geometry of an extreme arcjet ablated HEEET (heatshield for Extreme Entry Environment Technology) pattern developed by NASA and subject to the recent roughness study by Wilder and Prabhu [23] [24] and an idealised two-dimensional saw-tooth pattern with a 25 degree windward angle (ST25). Figure. 6 shows the topography of roughness and the θ_{Rn} distribution for an adjacent peak and trough of the HEEET like pattern. Similarly, Fig. 7 shows ST25 pattern and dimensions.

Parameter	Symbol	Value
Normal Emissivity	ε	0.88
Density	ρ	1.18gcm^{-3}
Specific Heat Capacity	c	$1.408\text{Jg}^{-1}\text{K}^{-1}$
Thermal Conductivity	k	$0.175\text{Wm}^{-1}\text{K}^{-1}$
$\sqrt{\rho ck}$		541

Table 1 Gloss finish VeroBlack material properties.

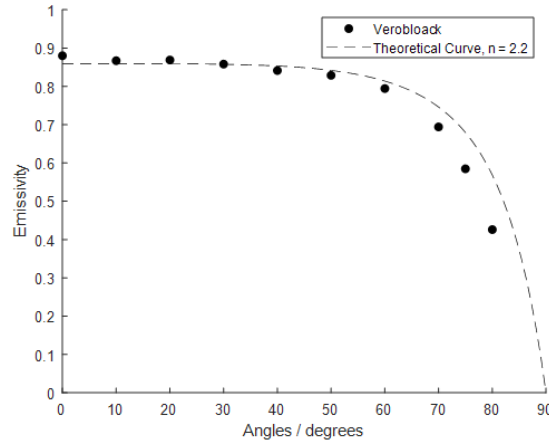


Fig. 8 Experimentally obtained emissivity curve for the Vero-black 3D printed material compared to a dielectric material with refractive index 2.2.

As mentioned earlier, the operation of HDT produces a number of periods of steady total pressure and unit Reynolds number. The condition 1 refers to the first of these periods, condition 2 to the second, and so on. At each instance, the free stream properties were evaluated from the pitot pressure, total temperature and nozzle supply static pressure recorded by surface instrumentation on the model and tunnel instrumentation. The nominal free stream conditions over 4 conditions used are detailed in Table. 2. Note that these are nominal and shot-to-shot variations in flow conditions were counted for during the processing of the data. It is also of note, that a nitrogen free stream was used as the carbon dioxide present in air absorbs a significant amount of radiation within the wavelength range of the camera used.

Parameter	Units	C1	C2	C3	C4
M_∞	-	5.00	5.00	5.00	5.00
p_0	kPa	3844	2977	2334	1839
p_∞	kPa	7.2	5.6	4.4	3.5
T_0	K	428.1	410.2	389.8	374.8
T	K	71.3	68.3	64.9	62.5
u_∞	ms^{-1}	847	829	808	792
ρ_∞	kgm^{-3}	0.35	0.29	0.24	0.19
Re_x	$10^6 m^{-m}$	62	51	44	37

Table 2 Free stream conditions.

C. IR Camera Set Up

The images were captured with a Telops FAST M3K mid-wave infrared (MWIR) camera with a 100mm focal length lens mounted with a 19.05mm thick extension ring at a working distance of 520mm providing a resolution of approximately 7pixelsmm^{-1} over a $38\times 46\text{mm}$ FoV. During the experiments, the camera was positioned in two different orientations relative to the flat plate model shown by the schematic in Fig. 9. The IR camera imaged the roughness geometry in both orientations at a significant distance downstream of the start of the pattern such that any roughness effects were fully established within its FoV.

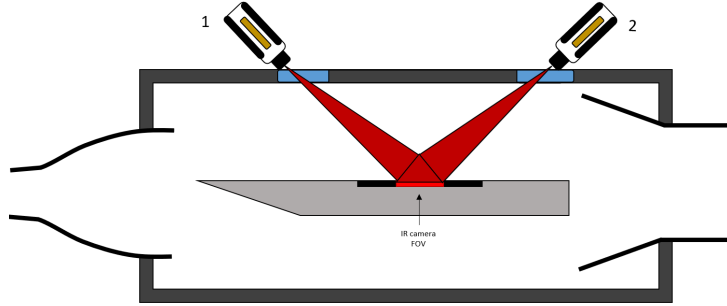


Fig. 9 Schematic showing the two positions the IR camera was placed relative to the flat plate model inside the test section during the test campaign.

The IR target plate was produced following a similar design philosophy as Cardone et al. [19]. A target consisting of an FR2 composite copper coated strip board with 1mm diameter holes at regularly spaced intervals of 2.5mm was used. The board was then backed by a 2mm thick aluminium piece painted matte black. This combination of materials meant that target heated quickly and that there was a strong contrast between the hot, high-emissivity painted surface and the reflective surface of the copper coating. The target captured by the IR camera in two orientations is shown in Fig. 10, highlighting the strong contrast between the control points and the reflective surface.

Using the methodology described in Section IV.A, the intrinsic and extrinsic parameters of the camera were determined. The coordinates of the target in the world frame were defined by setting the origin as the top-leftmost marker, and then, due to the regular spacing, the rest were defined relative to that marker. Their image coordinates in pixels were evaluated using a two-stage circular Hough transform [25] [26]. From these coordinate points, the following θ_{flat} distributions shown in Fig. 11 of the two IR views were found.

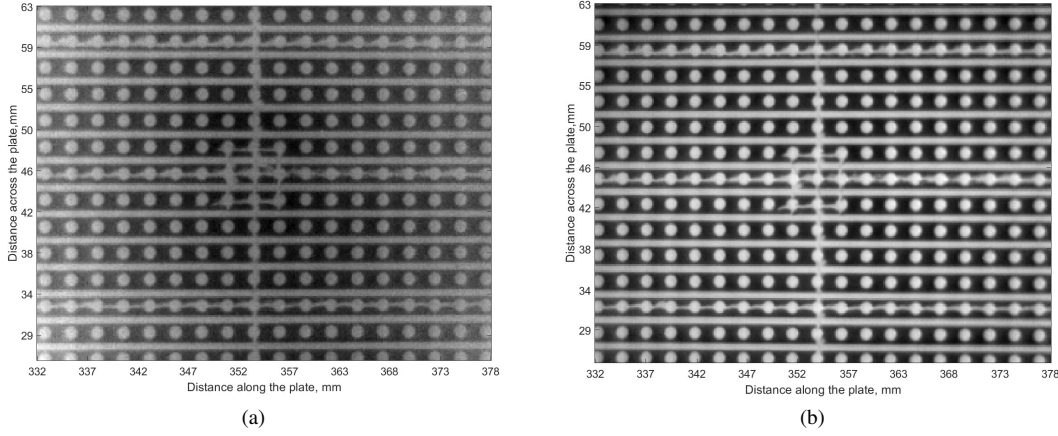


Fig. 10 (a) IR target plate imaged with the IR camera in position one (b) IR target plate imaged with the IR camera in position two

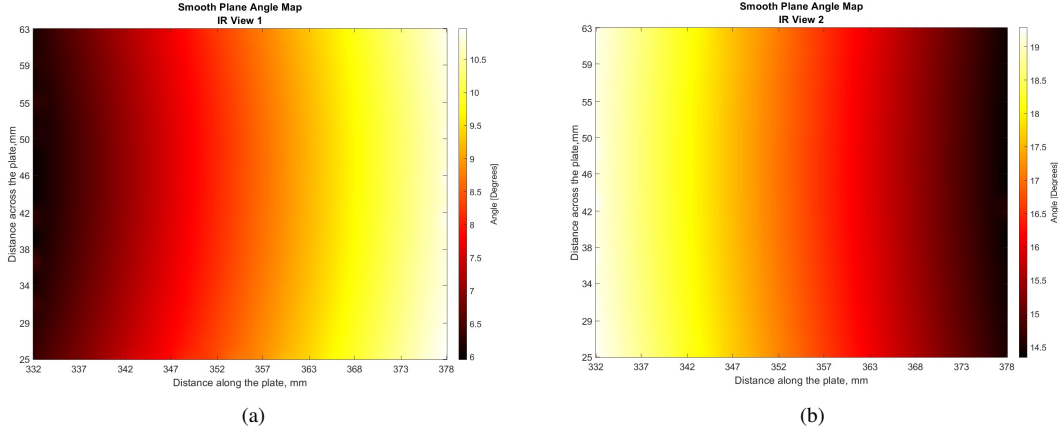


Fig. 11 (a) $\theta_{flat}(x, y)$ distribution evaluated with the camera positioned in IR view 1. (b) $\theta_{flat}(x, y)$ distribution evaluated with the camera positioned in IR view 2

VI. Post Processing

The form of the data output by the camera details the raw counts received by it during recording. Section III.A details the conversion of this data to temperature data using a black body calibration and the materials emissivity. To convert this to heat flux, further processing is required. As the temperature observed by each pixel is known throughout the duration of the recorded time, the temperature change seen by the surface is easily evaluated. At this stage, the signal will have some high frequency noise contaminating the temperature trace, and so it is sent through a low pass filter. With the high frequency noise removed, the signal is then passed through a fast Fourier transform based finite impulse response filter whose coefficients are defined by an impulse response function. This method implicitly applies a semi-infinite assumption, as the impulse response function is generated through the deconvolution of two basis functions, a unit step of heat flux in time and the corresponding parabola response in temperature. To then convert the heat flux data to Stanton number the following relationship, shown in Eq. (17), was used.

$$St = \frac{q_{IR}}{\rho_{\infty} u_{\infty} \cdot (h_e - h_w)} \quad (17)$$

Where ρ_{∞} refers to the free stream static density and u_{∞} to the free stream velocity, h_e and h_w refer to the enthalpy at the boundary layer edge and wall respectively. The enthalpy at the boundary layer edge was evaluated from the

recovery temperature which in turn was evaluated using the usual definition in Eq. (18).

$$T_r = T_\infty \cdot \left[1 + r \left(\frac{\gamma + 1}{2} \right) \cdot M_\infty^2 \right] \quad (18)$$

Here r refers to the recovery factor taken as $r = Pr^{\frac{1}{3}}$ for turbulent flows

VII. Results

The IR data and gauge data given showcase the Stanton number enhancement evaluated by taking the Stanton number distribution of the rough surface and normalising it the Stanton number distribution of the smooth surface (St_0). Additionally, all IR images shown are evaluated at condition 2, and as the instrumentation on the roughened surfaces are visible in the full FoV of the camera for both the geometries, a central section was selected, expanding 20mm in width and the full length of the original view.

A. HEEET Pattern Data

As stated, finding the discrepancy in degree of heating received by different sections of the roughness pattern allows for the identification of those sections within the IR camera's FoV. Subsequently, the θ_{Rn} value from the angle distribution shown in Fig. 6(b) can be found. This value then augments that pixels θ_{flat} value found through the optical calibration process detailed in Section IV. With the camera angle of each pixel known, the emissivity can then be found simply by utilising the emissivity calibration curve shown in Fig. 8. The result shown in Fig. 12 was obtained with the camera in IR position one.

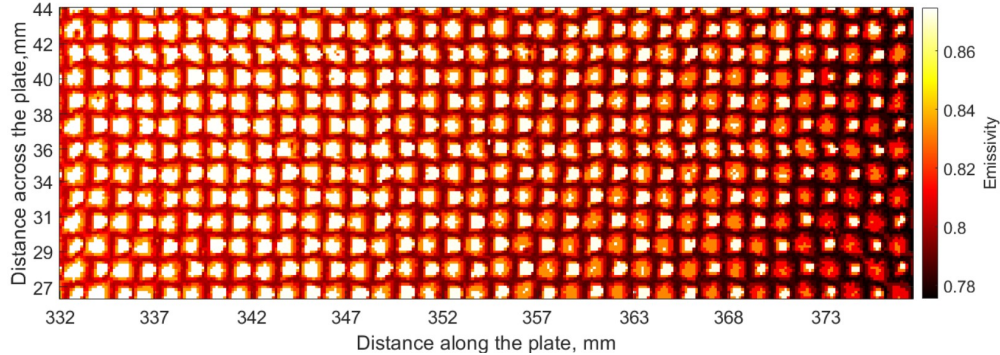


Fig. 12 Emissivity map for the HEEET like roughness pattern with a pixel resolution of 7 pixels per millimeter.

Using this emissivity data, the heatflux, and then Stanton number, enhancements were evaluated. Figure. 13 shows the Stanton number enhancement map that the IR camera captured whilst observing the HEEET-like pattern. It can be seen that the peaks of the pattern experience approximately twice the heating than the aerodynamically smooth surface received — a much higher degree of heating compared to the troughs of the roughness pattern that experienced comparable or slightly lower heating than the smooth control surface.

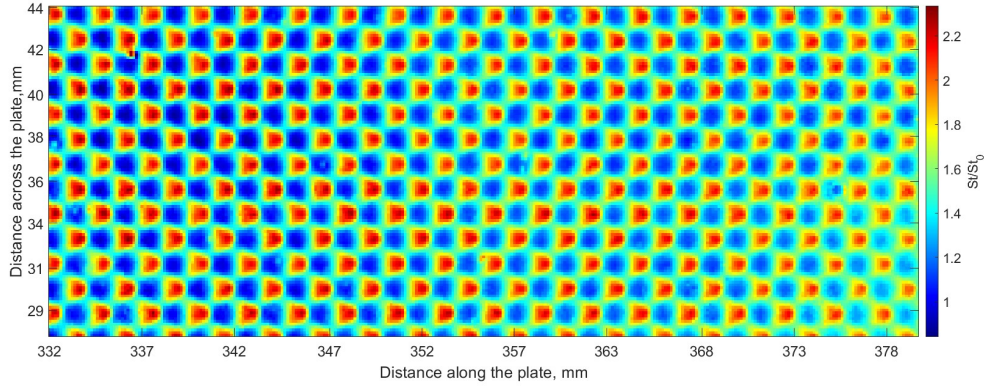


Fig. 13 The Stanton number enhancement experienced by the HEEET like roughness pattern when subject to hypersonic flow compared to a aerodynamically smooth surface.

On the highly-curved surfaces of the roughness geometry, an emissivity drop as great as 11% from the value normal to the surface is observed. Passing this emissivity difference through the post-processing results in a not insignificant percentage difference of around 9% in the heat flux data obtained. Fig. 14 shows the percentage difference map between the emissivity corrected heat flux data and the data evaluated assuming a constant emissivity.

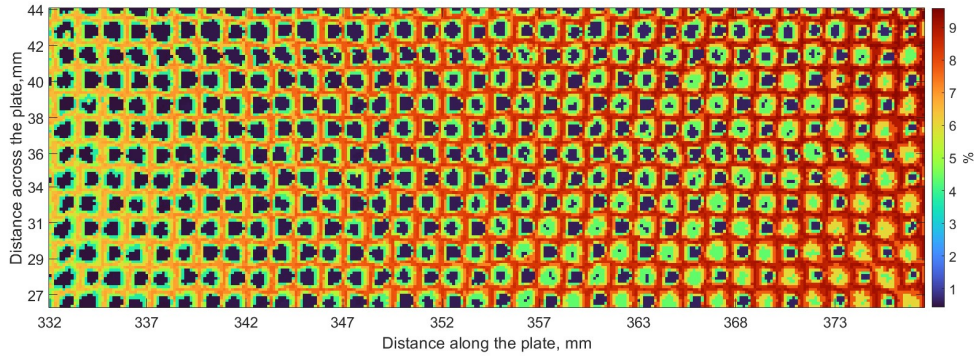


Fig. 14 The percentage difference between the emissivity corrected heat flux data and the heat flux data assuming a constant emissivity for the HEEET like pattern.

Lastly, calorimeter gauge data was collected alongside the IR data for the HEEET pattern. Figure. 15 displays the discrete data points acquired over the surface by the gauges compared to the IR signal against the unit Reynolds number. It can be seen that the Stanton number enhancement measured by the calorimeter gauges at a location along the plate contained within the IR FoV remain close in magnitude. The gauges that are outside the FoV are within the maximum and minimum signal acquired by IRT. Additionally, it also showcases the limitation of gauge methods as the discrete data points of the gauges fail to capture full profile of the roughness geometry, a limitation that IRT surpasses.

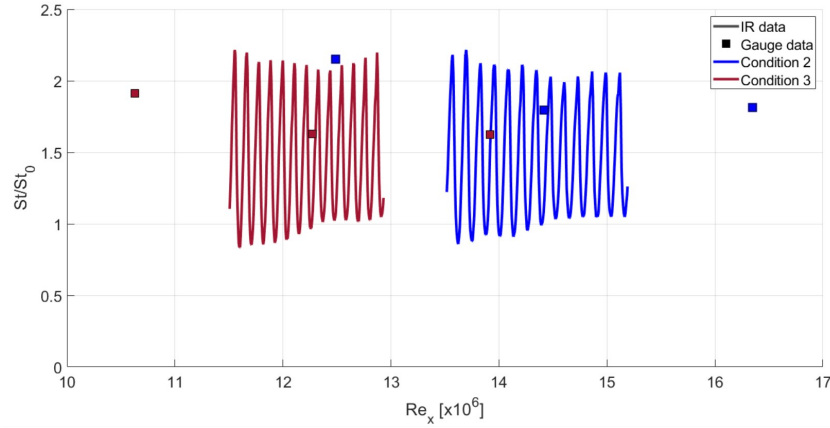


Fig. 15 Comparison of IRT to calorimeter Stanton number enhancement over plotted against Re_x for the HEEET like roughness pattern for Condition 2 and 3.

B. ST Pattern Data

The emissivity map generated for the ST25 geometry is shown is displayed in Fig. 16. Each saw-tooth possess a $200\mu\text{m}$ radius fillet As shown in Fig. 7(b). Due to its size and the resolution of the camera set up, the surface angle variation over this feature could not be captured and so an assumption of a flat surface was applied in both IR views. In IR view 2, the camera observed the leeward surface at a minimum angle of 65 degrees. From simply trigonometry the projected length of the leeward surface was found to range from approximately 4-6 pixels over the whole IR FoV.

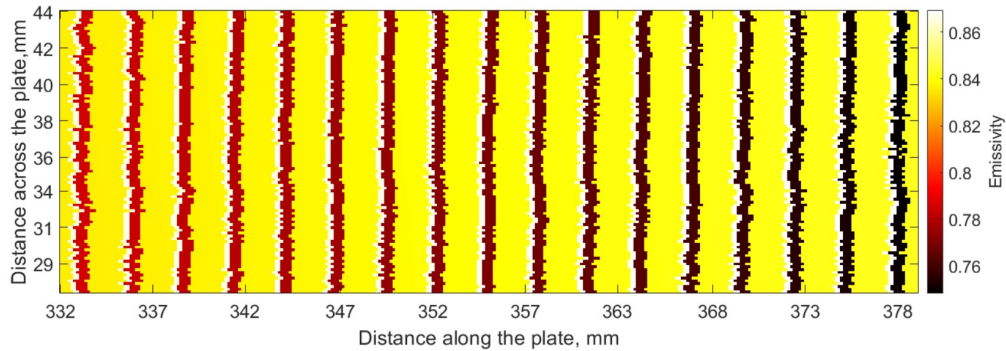


Fig. 16 Emissivity map for the ST25 viewed in position 2 with a pixel resolution of 7 pixels per millimeter.

The Stanton number enhancement measured by the IR camera over the two-dimensional roughness geometry using the emissivity map displayed above is shown in Fig. 17. Again, it is shown that the peaks of the pattern were subject to a greater degree of heating, seeing around twice the degree experienced by the smooth surface.

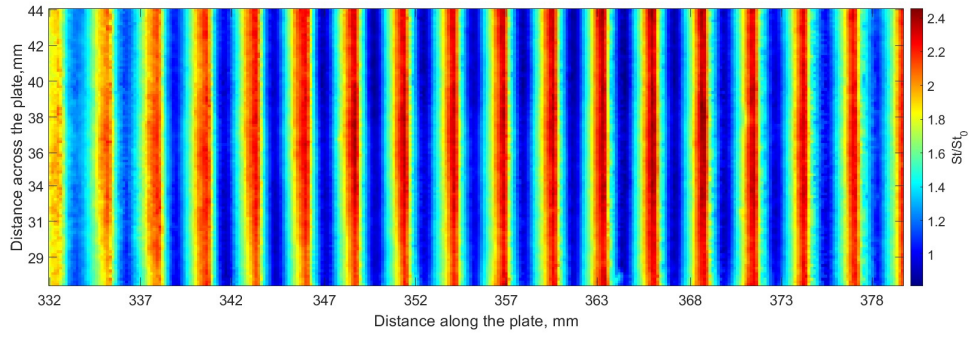


Fig. 17 Stanton number enhancement experienced by ST25 pattern compared to an aerodynamically smooth surface viewed in position 1.

From Fig. 16 the leeward surface is seen to have experienced the largest change in emissivity, reaching a difference of around 13% at the right most end of the camera's FoV. A comparison of the resulting heat flux evaluated using a constant emissivity to that evaluated using the emissivity map in Fig. 16 highlighted a maximum variation of 16% on the leeward surface. Along the windward face of the pattern, a much smaller percentage difference was observed at around 4%. This is of course due to the camera view angle being significantly below the critical 50 degree point, producing a change in emissivity of approximately 2%. The resulting percentage difference over a section of the IR camera's FoV is shown in Fig. 18.

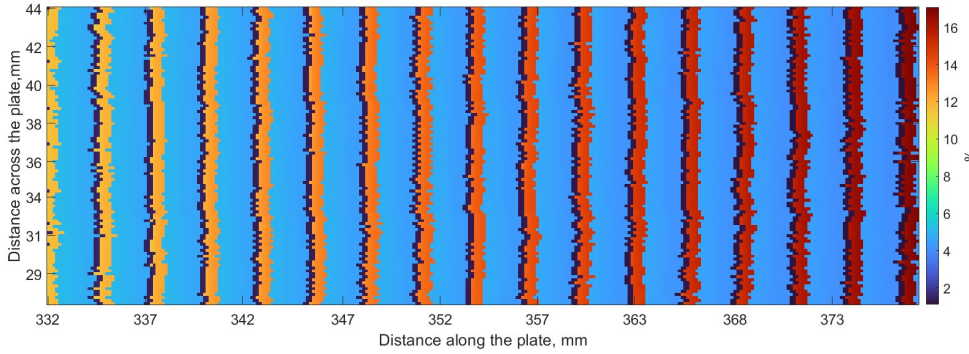


Fig. 18 The percentage difference between the emissivity corrected heat flux data and the heat flux data assuming a constant emissivity for ST25 viewed in position 2.

Similarly, a comparison of the emissivity corrected IRT Stanton number enhancement data to that of the thin film gauges on the same surface was made. Figure. 19 showcases the data from both techniques with the camera position in view 1 over a single roughness element for 4 of the steady total pressure conditions. IR data curves are produced by a line trace over the width of camera's FoV. We can see that they are in reasonable agreement with one another around the peak of the roughness pattern for conditions 1-3, with the IRT data failing to match magnitude of the spike seen in condition 4. Furthermore, the minimum signal recorded by the IRT is higher than that of the thin TFG data.

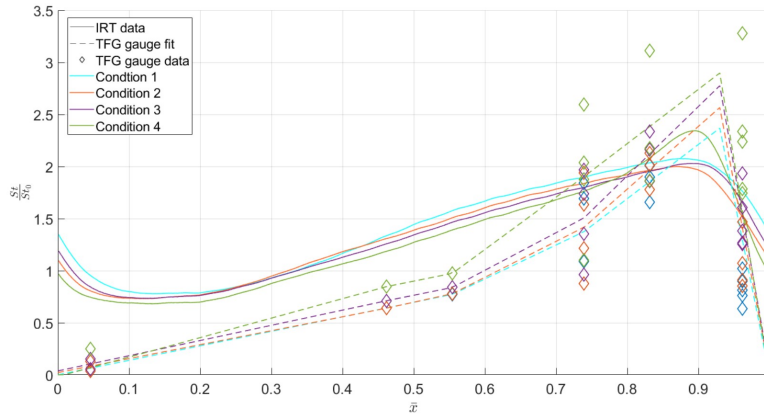


Fig. 19 Comparison of IRT to TFG Stanton number enhancement over a single saw-tooth element.

VIII. Conclusion

A methodology to adapt the optical technique of infrared thermography for use on rough walls has been presented that corrects for the emissivity of the material. The three-dimensional nature of rough surface that is inherently lost when captured by the IR camera is retrieved utilising the optical calibration process provided by Heikkila and the relationship between the roughness height and heat flux. This then allows information about surface angles to be laid over the image, and thus the emissivity of the surface at each pixel to be calculated. The results displayed showcased the importance of evaluating directional emissivity as the heat flux determined by IRT swayed by amounts greater than 10% on the steeper sections of the roughness geometries. Furthermore, a comparison between the Stanton number enhancement calculated using thin film gauges to that calculated using IRT revealed that they were in reasonable agreement with one another, disagreeing only on the minimum heat flux experienced and on the peak heat flux on one of the four conditions. Lastly, it is of note that the resolution of the set-up presents itself as a limitation, the more pixels per unit length the more precisely the pixel location can be determined and the finer the generated emissivity map and vice versa.

Overall, the proceedings in this paper provide a means to obtain spatially continuous heat flux data over large-scale rough walls in a non-intrusive manner that can be easily adapted to any surface geometry. Ultimately, aiding research into rough wall effects over a wider range of possible rough surface topographies.

IX. Acknowledgements

The authors of this work would like to thank Dr. Luke Doherty and Mr. Tristan Crumpton for the maintenance and operation of the Oxford High Density Tunnel. Gratitude is extended to the Engineering and Physical Sciences Research Council for supporting the studentship of Wesley Condren, as well as to Mr. Jonathan Connolly for his invaluable insights and expertise.

References

- [1] Neeb, D., Gülham, A., and Merrifield, J. A., "Rough-Wall Heat Flux Augmentation Analysis Within the ExoMars Project," *Journal of Spacecraft and Rockets*, Vol. 163, No. 1, 2016.
- [2] Nikuradse, J., "Law of flows in rough pipes, English Translation," *NACA TM 1292*, 1950.
- [3] schlichting, H., "Experimental Investigation of the problem of surface roughness," *Technical Memorandum*, , No. 823, 1936.
- [4] R. DIRLING, J., "A method for computing roughwall heat transfer rates on reentry nosetips," *8th Thermophysics Conference*, AIAA, 2005. <https://doi.org/10.2514/6.1973-763>, URL <https://arc.aiaa.org/doi/abs/10.2514/6.1973-763>.
- [5] van Rij amd B J Belnap, J. A., and Ligrani, P. M., "Analysis and Experiments on Three-Dimensional, Irregular Surface Roughness," *Journal of Fluids Engineering*, Vol. 124, No. 3, 2002, pp. 671–677. <https://doi.org/10.1115/1.1486222>.
- [6] Sigal, A., and Danberg, J. E., "New correlation of roughness density effect on the turbulent boundary layer," *AIAA Journal*, Vol. 28, 1990, pp. 554–556. <https://doi.org/10.2514/3.10427>.

- [7] Holden, M., Wadhams, T. P., and Mundy, E. P., *A Review of Experimental Studies of Surface Roughness and Blowing on the Heat Transfer and Skin Friction to Nostips and Slender Cones in High Mach Numbers Flows*, AIAA, 2008. <https://doi.org/10.2514/6.2008-3907>, URL <https://arc.aiaa.org/doi/abs/10.2514/6.2008-3907>.
- [8] Naved, I., Hermann, T., Hambidge, C., Ifti, H. S., Falsetti, C., and McGilvray, M., "Transpiration Cooling Heat Transfer Experiments in Laminar and Turbulent Hypersonic Flows," *AIAA*, 2022.
- [9] Carlomagno, G. M., and Cardone, G., "Infrared thermography for convective heat transfer measurements," *Experiments in Fluids*, 2010. <https://doi.org/10.1007/s00348-010-0912-2>.
- [10] Ress, T. W., Fisher, T. B., Bruce, P. J. K., Merrifield, J. A., and Quinn, M. K., "Experimental characterisation of the hypersonic flow around a cuboid," *Experiments in Fluids*, 2020.
- [11] Naved, I., Hermann, T., McGilvray, M., Rocher, M. E., Hambidge, C., Doherty, L., Page, L. L., Grossman, M., and Vandeperre, L., "Heat Transfer Measurements of a Transpiration Cooled Stagnation Point in Transient Hypersonic Flow," *AIAA*, Vol. 53, 2020.
- [12] Dewitt, D. P., Bergman, T. L., and Lavine, A. S., *Fundamentals of Heat and Mass Transfer*, 6th ed., John Wiley Sons Inc., River Street Hoboken USA, 2007.
- [13] Mirko Zaccara, J. B., and Cardone, G., "A general procedure for infrared thermography heat transfer measurements in hypersonic wind tunnels," *International Journal of Heat and Mass Transfer*, Vol. 53, 2020.
- [14] Astarita, T., and Carlomagno, G. M., *Infrared Thermography For Thermo-fluid-dynamics*, Springer, New York, 2013. <https://doi.org/10.1007/978-3-642-29508-9>.
- [15] Baehr, H., and Stephan, K., *Heat and Mass Transfer*, 5th ed., Waerme- und Stoffuebertragung, Germany: N. p., 2006. <https://doi.org/10.1007/3-540-32510-7>.
- [16] Heikkila, J., and Silven, O., "A four-step camera calibration procedure with implicit image correction," *Proceedings of IEEE Computer Society Conference on Computer Vision and Pattern Recognition*, 1997, pp. 1106–1112. <https://doi.org/10.1109/CVPR.1997.609468>.
- [17] Heikkila, J., "Geometric camera calibration using circular control points," *IEEE Transactions on Pattern Analysis and Machine Intelligence*, Vol. 22, No. 10, 2000, pp. 1066–1077. <https://doi.org/10.1109/34.879788>.
- [18] Zhang, Z., "A flexible new technique for camera calibration," *IEEE Transactions on Pattern Analysis and Machine Intelligence*, Vol. 22, No. 11, 2000, pp. 1330–1334. <https://doi.org/10.1109/34.888718>.
- [19] Cardone, G., Ianaro, A., dello Ioio, G., and Passaro, A., "Temperature maps measurement of 3D surfaces with infrared thermography," *Experiments in Fluids*, 2012.
- [20] Gao, X.-S., Hou, X.-R., Tang, J., and Cheng, H.-F., "Complete Spltion Classification for the Perspective-Three-Point Problem," *IEEE Transactions on Pattern Analysis and Machine Intelligence*, Vol. 25, No. 8, August 2003, pp. 930–943.
- [21] Wylie, S., Doherty, L., and McGilvray, M., "Commissioning of the Oxford High Density Tunnel (HDT) for boundary layer stability measurements at Mach 7," *2018 Fluid Dynamics Conference*, American Institute of Aeronautics and Astronautics, 2018.
- [22] McGilvray, M., Doherty, L. J., Neely, A. J., Pearce, R., and Ireland, P., "The Oxford High Density Tunnel," *20th AIAA International Space Planes and Hypersonic Systems and Technologies Conference*, AIAA, 2015. <https://doi.org/10.2514/6.2015-3548>, URL <https://arc.aiaa.org/doi/abs/10.2514/6.2015-3548>.
- [23] Wilder, M. C., and Prabhu, D. K., *Rough-Wall Turbulent Heat Transfer Experiments in Hypersonic Free Flight*, 2019.
- [24] Stackpoole, M., Boghozian, T., Chavez-Garcia, J., Ellerby, D., Fowler, M., Gage, P., Gasch, M., Gonzales, G., Kazemba, C., Kellermann, C., et al., "Heatshield for Extreme Entry Environment Technology (HEET) Enabling Missions Beyond Heritage Carbon Phenolic," *National Space and Missile Materials Symposium (NSMMS) 2017*, 2017.
- [25] Yuen, H., J.Princen, J.Illingworth, and J.Kittler, "Comparative study of Hough transform methods for circle finding," *Image and Vision Computing*, Vol. 8, No. 1, 1990, pp. 71–77.
- [26] E.R.Davies, *Machine Vision: Theory, Algorithms,Practicalities*, 3rd ed., Morgan Kauffman Publishers., 2005.